RSC Advances

PAPER

View Article Online
View Journal | View Issue

Cite this: *RSC Adv.*, 2022, **12**, 7762

Template free-synthesis of cobalt–iron chalcogenides [$Co_{0.8}Fe_{0.2}L_2$, L = S, Se] and their robust bifunctional electrocatalysis for the water splitting reaction and Cr(VI) reduction†

Manzoor Ahmad Pandit,[a] Dasari Sai Hemanth Kumar,[a] Manigandan Ramadoss,[ab] Yuanfu Chen[b] and Krishnamurthi Muralidharan*[a]

The ease of production of materials and showing multiple applications are appealing in this modern era of advanced technology. This paper reports the synthesis of a pair of novel cobalt–iron chalcogenides [$Co_{0.8}Fe_{0.2}S_2$ and $Co_{0.8}Fe_{0.2}Se_2$] with enhanced electro catalytic activities. These ternary metal chalcogenides were synthesized by a one-step template-free approach *via* a hexamethyldisilazane (HMDS)-assisted synthetic method. Transient photocurrent (TPC) studies and electrochemical impedance spectra (EIS) of these materials showed free electron mobility. Their bifunctional activities were verified in both the electrochemical oxygen evolution reaction (OER) and in the electrochemical reduction of toxic inorganic heavy metal ions [Cr(VI)] in polluted water. The materials showed robust catalytic ability in the oxygen evolution reaction with minimum possible over potential (345 and 350 mV @ η10) as determined by linear sweep voltammetry and the lower Tafel values (52.4 and 84.5 mV dec^{-1}) for $Co_{0.8}Fe_{0.2}Se_2$ and $Co_{0.8}Fe_{0.2}S_2$ respectively. Surprisingly, both the materials also showed an excellent activity towards electrochemical Cr(VI) reduction to Cr(III). Besides the maximum current achieved for $Co_{0.8}Fe_{0.2}S_2$, a minimum value for the Limit of detection (LOD) was obtained for $Co_{0.8}Fe_{0.2}S_2$ (0.159 μg L^{-1}) compared to $Co_{0.8}Fe_{0.2}Se_2$ (0.196 μg L^{-1}). We tested the durability of catalysts, the critical factor for the prolonged use of catalysts, through the recyclability measurements of these materials as catalysts. Both the catalysts presented outstanding durability and balanced electro catalytic activities for up to 1500 CV cycles, and chronoamperometry studies also confirmed exceptional stability. The enhanced catalytic activities of these materials are ascribed to the free electron movement, evidenced by the increased TPC measured and EIS. Therefore, the template-free synthesis of these electro catalysts containing non-noble metal illustrates the practical approach to develop such types of catalysts for multiple functions.

Received 21st January 2022
Accepted 22nd January 2022

DOI: 10.1039/d2ra00447j

rsc.li/rsc-advances

1. Introduction

Energy conversion through photo- or electro catalytic water splitting is a promising method to supplement depleting energy sources. In this water splitting, the half-reactions involved are hydrogen evolution (HER) and oxygen evolution (OER) reactions. The catalysts based on noble metals like Pt, RuO_2, or IrO_2 perform well in electrocatalytic water splitting.[1,2] However, the high cost and low abundance in Earth's crust prevents their large-scale utility.[3,4] Over the years, scientists have been engrossed in developing an efficient catalyst for the OER from water as it is the most favourable for green and cheap energy production.[5–8] Therefore, the focus is on readily available transition metals, which are cheap and less toxic, and their efficiency should match that of Pt or other noble metal catalysts.[9–11] Various transition metal compounds are active for electro catalytic OER performance.[12–17] The materials such as alloys, phosphides, carbides, selenides, borates, nitrides, carbon-based materials, and hydroxides are also used effectively as the OER catalysts.[18–25]

There are continuous investigations on the use of active transition elements like Ni, Co, Fe, Cu, and Mo and their combinations with sulphur as electro catalysts. Some varieties include Co–Ni–S,[26–29] Cu–Co–S, and Cu–Mo–S,[30–32] Co–Fe–S,[33–37] Co–Mo–S,[38] and Zn–Co–S.[39] The ternary chalcogenides have shown superior properties like high electrical conductance than monometallic due to the low activation energy for electron

[a]*School of Chemistry, University of Hyderabad, Hyderabad, India. E-mail: murali@uohyd.ac.in*

[b]*School of Electronic Science and Engineering, University of Electronic Science and Technology of China, Chengdu 610054, PR China*

† Electronic supplementary information (ESI) available: ESAS, UV-Vis DRS spectra, Data on controlled reactions and recyclability study and peak current study. See DOI: 10.1039/d2ra00447j

transfer between cations.[3] Apart from the stoichiometric combinations, distinct features such as the crystalline phase, morphology, and particle size influence the electro catalytic activity of transition metal sulfides.[16,17,40–42] Shen *et al.* reported a composite formation between cobalt–iron sulphide and nitrogen-doped mesoporous graphitic carbon ($Co_{0.5}Fe_{0.5}S$@N-MC) employing a simple soft template scheme. The covalently bonded nanostructures on a mesoporous graphitic layer in this material played the catalytic role in water oxidation reactions.[43] Consecutively, the transition metal chalcogenides have emerged as elegant OER electro catalysts.

Metal selenides are better than sulphides in many aspects as they possess more metallic character than sulphides and outstanding electrochemical properties.[44–47] Many transition metal selenides of the type MSe_2 (here M = Fe, Co, Mo, Ni, Cu, and Mn) were used as an electrode in energy conversion or storage devices such as solar cells, battery, super capacitor, fuel cells, sensors, and in water-splitting reactions (HER and OER).[48–53] Xiao *et al.* succeeded in depositing lamellar structured nanosheets of $CoSe_2$ on the Ti plate ($CoSe_2$NS@Ti) by an *in situ* method, and they used it directly as a cathode for superior hydrogen evolution activity.[54] An active strategy of attaining advanced properties in the nanoscale regime is doping CoSe2 crystal structure with another element with the same electronic configuration and atomic radius. This phenomenon will supplement defects/vacancies on an atomic scale by regulating the electrocatalytic active sites. Ramadoss *et al.* reported porous nanoarchitecture constructed by ultrathin $CoSe_2$ embedded Fe–CoO nanosheets acted as an excellent electrocatalyst material for water oxidation.[55] Zhao *et al.* reported synthesizing ultra-small $FeSe_2$ nanoparticles by a high-temperature solution-based method that acted as an excellent material for sodium-ion storage.[56] Sakthivel *et al.* claimed hydrothermal synthesis of $CoFeSe_2$/f-CNF and its use to detect caffeic acid electrochemically.[57] Yiqing *et al.* reported sulfidation and selenation of cobalt–iron by the hydrothermal method as the precursors to produce the Prussian-blue-analog (PBA) nanocubes and used them as excellent electrodes for dye-sensitized solar cells.[58]

On the other side, the continuous elimination of toxic and harmful chemicals from industrial effluents is detrimental to the environment. Many poisonous and carcinogenic chemicals released into the atmosphere significantly affect both aquatic as well as terrestrial life. The water bodies contaminated with such carcinogenic and toxic chemicals, including organic dyes [*e.g.*, rhodamine B, methylene blue dyes, nitro compounds][59–62] and toxic inorganic chemicals [*e.g.*, Cr(VI)][63] are unfit for drinking and other purposes. Therefore, the challenge is to develop such catalysts that are easily accessible, cheap, and their precursors must be abundant. Thus, the need is to develop highly efficient and stable catalysts to perform multirole in water splitting and detoxify toxic organic/inorganic chemicals.

Since electro catalysis depends on the unrestricted mobility of electrons, the environment around the nanocatalyst should promote electron movement rather than behaving as an insulator.[64] Moreover, chemical reactions occur on the catalyst's surface. To use metal chalcogenides as catalysts in any reaction, their active centres at the surface should be free from any hindrance and exposed to the interaction with the substrate. Although many reports documented sulphides and selenides as catalysts, the effect of clean surfactant-free surfaces on ternary chalcogenide systems without insulating effect and their bifunctional role in catalysis is not being probed. Besides the template free approach, the morphology and size of the catalyst are also the deciding parameters for superior catalysis. Primarily, morphological nanostructures having open access to their active sites are remarkably the most suitable bifunctional catalysts for sensors, OER and reduction of toxic chemicals.[65] Thus, a facile technique to develop and produce bifunctional ternary metal chalcogenides is highly imperative.

Inspired by the literature mentioned above and the results obtained herein, we report a study on transition metal chalcogenides ($Co_{0.8}Fe_{0.2}S_2$ and $Co_{0.8}Fe_{0.2}Se_2$) as bifunctional electro catalysts. The materials had no residual organic moieties resulting from the synthetic process. The materials were produced *via* hexamethyldisilazane (HMDS) – assisted self-template synthesis and characterized using various analytical and spectroscopic techniques.[66,67] The outstanding catalytic activities of the materials ($Co_{0.8}Fe_{0.2}S_2$ and $Co_{0.8}Fe_{0.2}Se_2$) were delineated from the electrochemical oxygen evolution reaction (OER). Besides the above catalytic pathways, electrochemical Cr(VI) reduction using $Co_{0.8}Fe_{0.2}S_2$ and $Co_{0.8}Fe_{0.2}Se_2$ materials is ample proof of their dual catalytic behaviour. There are no reports yet published about such types of bifunctional catalytic activities involving this material. Therefore, the present work establishes an attractive approach in developing non-noble metal and template free catalysts with multiple roles.

2. Experimental section

2.1. Materials

Cobalt chloride ($CoCl_2$ anhydrous), ferric chloride ($FeCl_3$ anhydrous), thiourea [$H_2NC(S)NH_2$], selenium powder, hexamethyldisilazane [$(Me_3Si)_2NH$] (HMDS), $K_2Cr_2O_7$, ethanol and Nafion were purchased from Sigma Aldrich. Distilled water was used for both the electrocatalytic pathways. The above-enlisted chemicals were of analytical grade and used as such.

2.2. Instrumentation

The synthesized materials were subjected to various analytical techniques for their characterization. The crystal structure and phase purity were confirmed using PXRD patterns obtained from Bruker D8 (CuKα, λ = 1.54056 Å, 2θ = 20° to 70°) spectrometer. The morphology and elemental distribution of synthesized materials were performed by FESEM (Ultra 55 Carl Zeiss microscopy with operating voltage = 10 kV), TEM (FEI Technai G2 F20 STEM with a 200 kV) and EDAS studies. Optical properties were performed using the JASCO-V770 UV/Vis spectrophotometer. The nitrogen adsorption–desorption isotherms and the pore distribution of materials were estimated by the Brunauer–Emmett–Teller instrument (BET) (Nova 2000e, Quantachrome Instruments Limited, USA using liquid nitrogen (77 K)). The oxidation states of elements and the chemical composition were determined by X-ray photoelectron

spectroscopy (XPS) (Thermo scientific Escalab 250Xi spectrometer with Al-Kα radiation). Electrochemical studies were carried using Ametek PARSTAT electrochemical workstation in a conventional three-electrode system. Transient-photocurrent (TPS) studies and electrochemical impedance spectra (EIS) were performed by Zahner-Zennium electrochemical work station using a three-electrode system.

2.3. Synthesis of $Co_{0.8}Fe_{0.2}S_2$ and $Co_{0.8}Fe_{0.2}Se_2$ chalcogenides

The wet chemical synthesis of $Co_{0.8}Fe_{0.2}S_2$ nanoparticles was achieved by hexamethyldisilazane (HMDS) – assisted method with slight modification. In a typical reaction, 1.54 mmol of $CoCl_2$ and 0.31 mmol of $FeCl_3$ were added one by one into a two-neck RB connected to Schlenk lines and purged with N_2 gas. Then HMDS (6 mL) was injected using a syringe under the continuous nitrogen gas supply to maintain the inert condition. The reaction mixture was stirred for 30 minutes to dissolve precursor salts in the medium at 40 °C; after 30 minutes, 3.08 mmol of thiourea was added. The reaction was set to reflux at 160 °C for 3 hours with continuous stirring. After completing the reaction, the precipitate was separated by centrifugation (set) at 2500 rpm, washed by deionized water and ethanol every 3–4 times to get the desired product. The material collected was subjected to a high vacuum at 70 °C overnight to remove any residual solvents. A similar procedure was applied to the synthesis of $Co_{0.8}Fe_{0.2}Se_2$. The same precursors of cobalt and iron were used while thiourea was exchanged for selenium powder (3.08 mmol) to produce ternary metal selenide.

2.4. Transient photocurrent (TPC) and electrochemical impedance spectra (EIS)

The three-electrode system used for TPC and EIS consists of an FTO plate loaded with the synthesized materials as a working electrode, Pt as a counter electrode, and Ag/AgCl electrode as a reference. The working electrode was prepared by mixing 5 mg of synthesized materials ($Co_{0.8}Fe_{0.2}S_2$ or $Co_{0.8}Fe_{0.2}Se_2$) and 40 μl of Nafion (binder) in an 8 : 2 ratio water:ethanol solution. This mixture was sonicated to form a homogenous mixture and then drop-cast on an FTO glass plate to form a square-like thin film. The other portion of FTO was covered with Teflon tape and allowed to dry in an oven at 60 °C until the solvent was evaporated. The sodium sulphate solution 0.1 M was used as an electrolyte. For transient photocurrent studies, the plot of photocurrent against time during light on/off cycles with the time interval of 20 s was recorded. A similar FTO loaded glass plate was used for carrying EIS studies. The EIS measurements were taken in a frequency range of 100 mHz to 100 kHz at open circuit potential with the amplitude of sinusoidal voltage equal to 10 mV.

2.5. Preparation of electro catalyst as working electrodes for OER and electrochemical measurements

Electrochemical OER performances were monitored using the electrochemical workstation (CHI 660D) at room temperature (298 K). A home-made setup with a three-electrode system was used consisting of a glassy carbon ($Co_{0.8}Fe_{0.2}S_2$ and $Co_{0.8}Fe_{0.2}Se_2$ modified and bare-GCE) as working electrode, Pt ring as the counter electrode, and a silver electrode as a reference electrode in 1 M KOH. Electro catalyst on GCE was loaded (~0.3 mg cm^{-2}) with Nafion binder *via* the drop-cast method with the micropipette assistance and then dried at the oven. All the electrochemical measurements were repeated many times to ensure consistency and reproductive performance. For the electrochemical performance evaluation, potentials of linear sweep voltammetry (LSV) and cyclic voltammogram (CV) were calibrated *vs.* reversible electrode (RHE as follows, $E_{RHE} = E_{obt} + E_{Ag/AgCl} + 0.059 \times pH$ V). LSV measurements (0.005 V s^{-1}, 1 to 1.8 V potential windows) were done to calculate onset over potential at current densities (j_{10}, 10 mA cm^{-2}) and Tafel plots (log(j) *vs.* V_{RHE}). Double-layer capacitance (C_{dl}) measurements were done using CV measurements between the V_{dl} windows 1.203 V to 1.302 V.

2.6. Electrochemical Cr(VI) reduction

Electrochemical reduction of Cr(VI) was carried using a conventional three-electrode system. Glassy carbon electrode (GCE), Ag/AgCl (3 M KCl), and Pt were used as working, reference and counter electrodes respectively. The potentials used in the experiments were from −0.2 V to 1 V. The electrochemical Cr(VI) reduction was initially performed with different acidic media solutions to check which one will produce maximum current. The electrolyte, which gives the highest current, was used for further experiments. Apart from this, different concentrations of Cr(VI) (0.01 μM to 50 μM) were also prepared for the other experiments. The limit of detection was calculated from the calibrated plot by using the formula shown in eqn (1) below.

$$\text{Limit of detection (LOD)} = 3 \times (s/m) \quad (1)$$

where s is the standard deviation of the calibrated plot and m is the slope of the regression equation.

3. Results and discussion

3.1. Synthesis and characterization

The hexamethyldisilazane (HMDS)-assisted synthesis has emerged as a robust method to produce binary metal chalcogenide nanoparticles without surfactant molecules.[66] In this work, the ternary materials, $Co_{0.8}Fe_{0.2}S_2$ and $Co_{0.8}Fe_{0.2}Se_2$, were synthesized utilizing the HMDS-assisted method with some modifications (Scheme 1). In this reaction, $FeCl_3$ and $CoCl_2$ were used as metal sources and thiourea or selenium powder as chalcogens to produce the desired sulphide and selenide materials. In both the reactions, HMDS acted as the solvent, reducing agent and surfactant molecule.[67] The entire process was accomplished using the Schlenk line through which nitrogen gas was purged continuously to maintain the inert atmosphere.

The crystal structure determination, together with phase purity, begins with powder X-ray difraction studies. Fig. 1 shows the well-established crystal structural information of $Co_{0.8}Fe_{0.2}S_2$ and $Co_{0.8}Fe_{0.2}Se_2$ chalcogenide materials. As shown

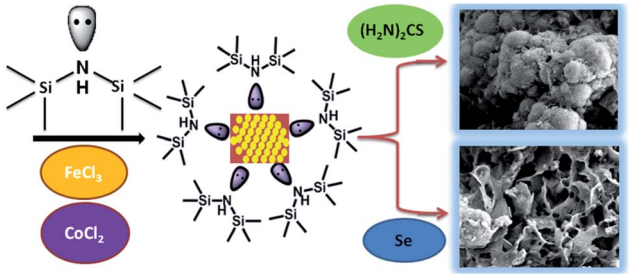

Scheme 1 Illustration of the reaction scheme carried for the synthesis of $Co_{0.8}Fe_{0.2}S_2$ and $Co_{0.8}Fe_{0.2}Se_2$ desired materials.

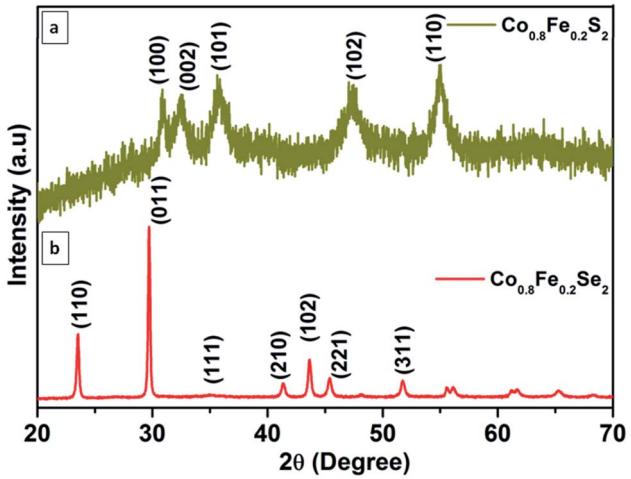

Fig. 1 PXRD of $Co_{0.8}Fe_{0.2}S_2$ and $Co_{0.8}Fe_{0.2}Se_2$ materials.

in Fig. 1a, all the peaks correspond to the hexagonal structure of $Co_{0.8}Fe_{0.2}S_2$ (JCPDS. No. 75-0607). The peaks at 2θ of 30.80°, 33.21°, 35.38°, 46.72°, and 54.64° can be indexed to planes of (100), (022), (101), (102) and (110) respectively. Likewise, Fig. 1b representing the diffraction spectra of $Co_{0.8}Fe_{0.2}Se_2$ has various intense peaks at 2θ values of 23.4°, 29.67°, 35.77°, 41.28°, 43.72°, 45.25° and 52.3° designated to crystal planes of (110), (011), (111), (210), (102), (221) and (311) respectively.[57] Besides this, the high-intensity peaks show the high crystalline nature of $Co_{0.8}Fe_{0.2}Se_2$. No other characteristic peaks are indexable to either pure CoS_2, $CoSe_2$, FeS_2 phases or any other stoichiometry of this trio in the PXRD spectra. Thus, confirming the single-phase and high purity of the material.

The X-ray photoelectron (XPS) spectrum (Fig. 2) of $Co_{0.8}Fe_{0.2}Se_2$ revealed its chemical composition and the valence oxidation states of elements in it. The survey spectrum (Fig. 2a) confirms the presence of Co, Fe, and Se in the material, besides the presence of C and O is indicative. As seen in Fig. 2b, the peaks related to Co $2p_{1/2}$ were appearing at 798.12 eV and 802.79 eV and the two other peaks at 782.90 eV and 786.31 eV. These peaks are the characteristics of Co^{3+} and Co^{2+}.[58] The XPS spectrum of Fe (Fig. 2c) shows peaks at 711.96 eV and 714.56 eV which are delineated with Fe^{2+} $2p_{3/2}$ and Fe^{3+} $2p_{3/2}$ respectively. In addition to these two peaks, another peak observed at 726.10

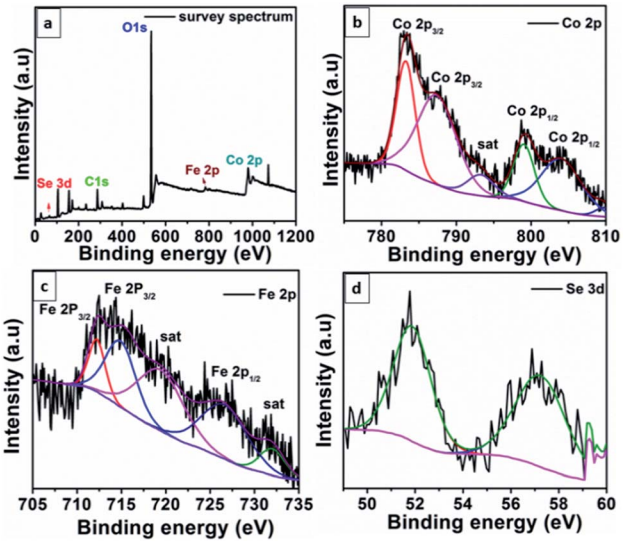

Fig. 2 The XPS spectrum of $Co_{0.8}Fe_{0.2}Se_2$. (a) Survey spectrum showing the presence of requisite elements. (b–d) The binding energy values for Co 2p, Fe 2p and Se 3d energy levels.

eV was characteristic of Fe $2p_{1/2}$.[57] The two satellite peaks obtained at the binding energies of 719.08 eV and 732.12 eV is an excellent proof for the existence of bivalence for Fe in $Co_{0.8}Fe_{0.2}Se_2$. The XPS spectrum of selenide (Fig. 2d) had two peaks at 52.06 eV for $3d_{5/2}$ and 57.30 eV for $3d_{3/2}$, respectively, indicating the existence of the metal–selenium bond.

3.2. Morphology and surface area

The FESEM and TEM images (Fig. 3 and 4) were investigated to ascertain the morphological metaphors of synthesized materials, while EDAS (Fig. S1†) was used to chalk out elemental

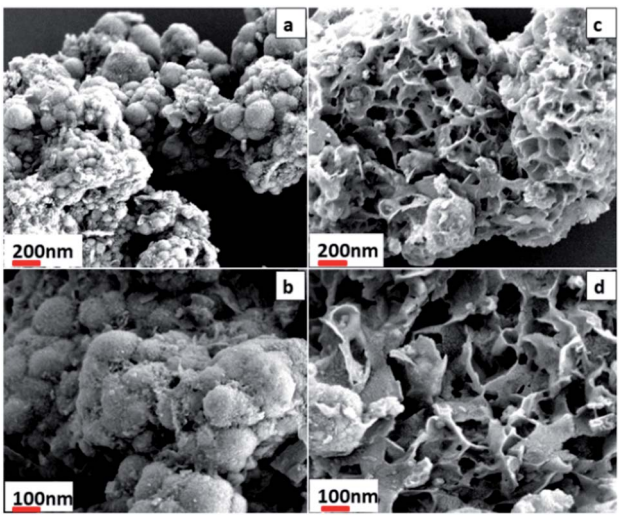

Fig. 3 The morphological analysis of chalcogenide materials. (a and b) Low and high magnification FESEM images of $Co_{0.8}Fe_{0.2}S_2$ showing sphere type morphology (c and d) low and high magnification FESEM images of $Co_{0.8}Fe_{0.2}Se_2$ showing flower type morphology.

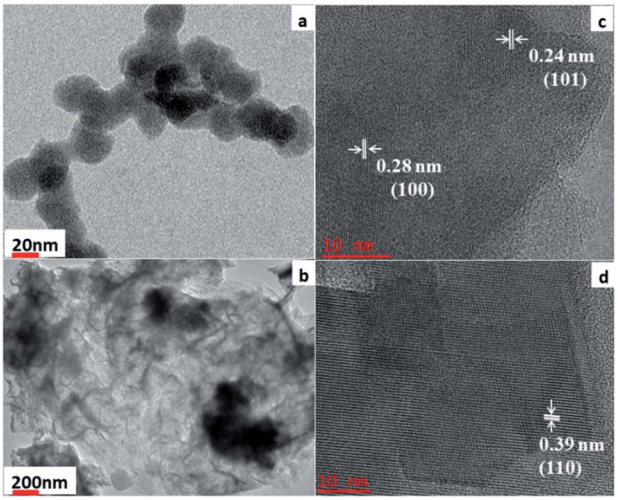

Fig. 4 The TEM images of $Co_{0.8}Fe_{0.2}S_2$ and $Co_{0.8}Fe_{0.2}Se_2$ (a and b) and HRTEM images (c and d).

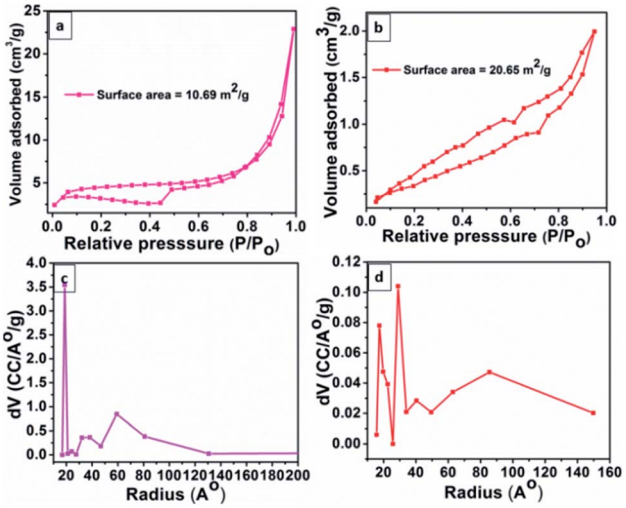

Fig. 5 Surface area analysis of (a) $Co_{0.8}Fe_{0.2}S_2$ and (b) $Co_{0.8}Fe_{0.2}Se_2$ materials. The pore radius of (c) $Co_{0.8}Fe_{0.2}S_2$ and (d) $Co_{0.8}Fe_{0.2}Se_2$.

analysis. Fig. 3a and b show that $Co_{0.8}Fe_{0.2}S_2$ particles acquired spherical morphology. The spheres outer surface looks like a loose texture type, probably because of the absence of an external surfactant in the synthesis process. As observed in both low and high magnification FESEM images, the spheres are fused. The average particle size determined for $Co_{0.8}Fe_{0.2}S_2$ was ~112 nm.

The Fig. 3c and d show flowers with flakes type morphology for $Co_{0.8}Fe_{0.2}Se_2$. Both low and high magnification FESEM reveal flower-like morphology delineated with thin flakes for $Co_{0.8}Fe_{0.2}Se_2$. Many spaces and porous surfaces are visible from the flowers showing that they can be promising materials for electrochemical processes. The elemental composition determined from EDAS (Fig. S1†) for both the materials exposed the good dispersal of elements Co, Fe, S, and Se. The TEM images (Fig. 4a and b) indicate that the materials show similar morphologies as in FESEM. The HRTEM images (Fig. 4c and d) show that the lattice fringes with *d*-spacing of 0.28 nm and 0.24 nm corresponding to (100) and (101) planes of $Co_{0.8}Fe_{0.2}S_2$, whereas the lattice fringes with *d*-spacing value 0.39 nm corresponds to (110) plane of $Co_{0.8}Fe_{0.2}Se_2$ respectively. The results obtained from HRTEM are therefore in good agreement with PXRD results of both $Co_{0.8}Fe_{0.2}S_2$ and $Co_{0.8}Fe_{0.2}Se_2$ respectively.

The present study aims to develop surfactant-free materials to exhibit excellent catalytic properties. The surface area of any material is the most crucial factor in explaining its catalytic activities. The specific surface area and pore size distribution were determined by studying BET isotherms. The Fig. 5a and b depict the N_2 adsorption–desorption isotherm of $Co_{0.8}Fe_{0.2}S_2$ and $Co_{0.8}Fe_{0.2}Se_2$ materials representing the specific surface area. The calculated surface area for $Co_{0.8}Fe_{0.2}S_2$ and $Co_{0.8}Fe_{0.2}Se_2$ was 10.69 and 21.41 $m^2\ g^{-1}$. Besides the surface area, the pore size distribution, as determined by BJH plots (Fig. 4c and d), was 18.753 Å and 17.147 Å for $Co_{0.8}Fe_{0.2}S_2$ and $Co_{0.8}Fe_{0.2}Se_2$ materials confirming the mesoporous nature of synthesized materials. The large surface area of $Co_{0.8}Fe_{0.2}Se_2$ materials shows that more active sites will be available, and hence more diffusion of electrolytic solution into pores will take place, thereby showing better catalytic performance.

3.3. Optical properties

The UV-Visible DRS spectra of $Co_{0.8}Fe_{0.2}S_2$ and $Co_{0.8}Fe_{0.2}Se_2$ revealed their optical properties (Fig. S2†). The absorption spectrum shows the materials absorbing mainly in the visible region with onset absorption at 260 nm. The broadband absorption was extending from 400 to 700 nm with maximum absorption at 650 nm. The broad absorption peak might be because of the morphological differences as we experience an inherent property shown by all the nanomaterials based on their size and shape. The energy bandgap (E_g) can be estimated from $(\alpha h\nu)^2$ *vs.* hν plot by projecting the straight line to hν axis were the point of intersection confirms the band value as shown in equation (2).[68]

$$\alpha h\gamma = A(h\gamma - E_g)^2 \quad (2)$$

In this equation, α represents optical adsorption constant, h is the Planck constant; ν is the frequency of light; E_g is the band edge value. From the DRS spectrum of these materials, the bandgap calculated were 1.52 eV for $Co_{0.8}Fe_{0.2}S_2$ and 1.57 eV for $Co_{0.8}Fe_{0.2}Se_2$. The low bandgap of spheres is because of quantum confinement, which results in a blue shift.

3.4. Transient photocurrent (TPC) and electrochemical impedance spectroscopy (EIS) studies

The TPC and EIS studies were carried on $Co_{0.8}Fe_{0.2}S_2$ and $Co_{0.8}Fe_{0.2}Se_2$ materials to understand the effect of clean and template free surfaces on electro catalytic properties. A three-electrode system, consisting of a conductive FTO glass plate on which the catalytic materials ($Co_{0.8}Fe_{0.2}S_2$ and $Co_{0.8}Fe_{0.2}Se_2$) were drop-cast to form a thin film acting as a working electrode, Pt as a counter electrode, and Ag/AgCl as a reference electrode,

was set up to study the TPC properties. The materials remain attached to FTO using Nafion as a binder, and the LED light (200 W) of wavelength 456 nm served as the source for visible light radiations. The 0.1 M sodium sulfate (pH 7) solution was used as the electrolyte solution.

When the $Co_{0.8}Fe_{0.2}S_2$ and $Co_{0.8}Fe_{0.2}Se_2$ materials were used in the dark, no photocurrent response was observed (Fig. 6a). A similar phenomenon was observed for blank FTO, but when loaded FTO was used, an appreciable photo response was observed when exposed to the visible light source. As shown in Fig. 6a with alternate on–off cycles, the spikes of transient photocurrent responses were observed for $Co_{0.8}Fe_{0.2}S_2$ and $Co_{0.8}Fe_{0.2}Se_2$ materials loaded on FTO. The photocurrent responses achieved were stable and with high intensity. The uniform and high transient photocurrent values indicate an efficient separation of photo excited charge carriers on the FTO glass loaded with $Co_{0.8}Fe_{0.2}S_2$ and $Co_{0.8}Fe_{0.2}Se_2$ materials.

The resistance to the flow of charge carriers and the recombination rate were investigated further by recording EIS. The EIS spectra were obtained at a frequency of 100 kHz and alternating current (AC) voltage amplitude of 10 mV with an open circuit potential of 1 V. The EIS results are represented by the Nyquist plot (Z imaginary *vs.* Z real) in Fig. 6b. From the Nyquist plots, it is observed that the smaller arc radius is obtained for $Co_{0.8}Fe_{0.2}S_2$ compared to $Co_{0.8}Fe_{0.2}Se_2$, showing that the interfacial charge transfer process is smooth and the resistance offered to the flow of charge carriers is less for $Co_{0.8}Fe_{0.2}S_2$ than $Co_{0.8}Fe_{0.2}Se_2$. The small size of arc radius of $Co_{0.8}Fe_{0.2}S_2$ indicates superior catalytic performance than $Co_{0.8}Fe_{0.2}Se_2$.

3.5. Electrocatalytic water splitting using $Co_{0.8}Fe_{0.2}S_2$ and $Co_{0.8}Fe_{0.2}Se_2$

The capabilities of $Co_{0.8}Fe_{0.2}S_2$ and $Co_{0.8}Fe_{0.2}Se_2$ materials as the catalysts in OER are evaluated by the LSV (Fig. 7a) and CV (Fig. 7c–f) measurements using a typical homemade three-electrode system. Highly reactive electro active sites were created on GCE by modifying it with $Co_{0.8}Fe_{0.2}S_2$ and $Co_{0.8}Fe_{0.2}Se_2$ to achieve an excellent oxygen evolution reaction (OER). The achieved over potential during LSV measurements was calculated as $E_{(RHE)}$ −1.23 V. As shown in Fig. 6a, $Co_{0.8}Fe_{0.2}Se_2$ (345 mV η @ 10 mA cm^{-2} and 425 mV η @ 50 mA cm^{-2}) resulted in relatively less over potential than $Co_{0.8}Fe_{0.2}S_2$ (350 mV η @ 10 mA cm^{-2} and 475 mV η @ 50 mA cm^{-2}). Whereas GCE results in negligible OER current indicating $Co_{0.8}Fe_{0.2}S_2$ and $Co_{0.8}Fe_{0.2}Se_2$ have strong OER catalytic ability. The low over potential resulting from the electrode modification demonstrated $Co_{0.8}Fe_{0.2}S_2$ and $Co_{0.8}Fe_{0.2}Se_2$ as unique types of electro catalysts.

Furthermore, $Co_{0.8}Fe_{0.2}Se_2$ precatalysts OER kinetics (Tafel plots) is also favourable towards OER and consistent with reports. It was derived from the Tafel equation as follows, $\eta = a + b \log |J|$ by fitting the linear portion of LSV curves.[35] Tafel plots (Fig. 7b) of $Co_{0.8}Fe_{0.2}Se_2$ (52.4 mV dec^{-1}) and $Co_{0.8}Fe_{0.2}S_2$

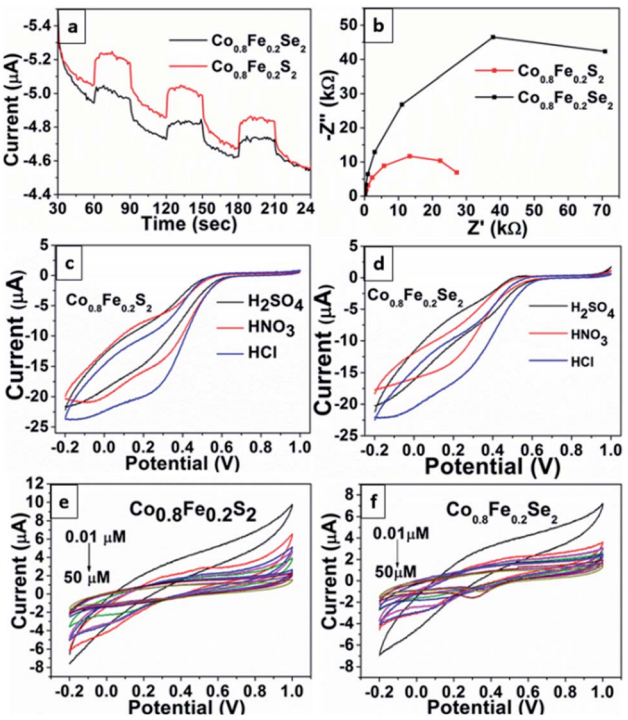

Fig. 6 (a and b) Transient photocurrent and impedance measurements (c and d) CVs obtained for 0.1 mM Cr(VI) in different acid electrolytes (H_2SO_4, HNO_3, HCl all 0.1 M) using GCE/$Co_{0.8}Fe_{0.2}S_2$ and $Co_{0.8}Fe_{0.2}Se_2$ at a scan rate of 10 mV s^{-1} (e and f) CVs of different Cr(VI) concentrations using GCE/$Co_{0.8}Fe_{0.2}S_2$ and $Co_{0.8}Fe_{0.2}Se_2$ at a scan rate of 10 mV s^{-1} in 0.1 M HCl.

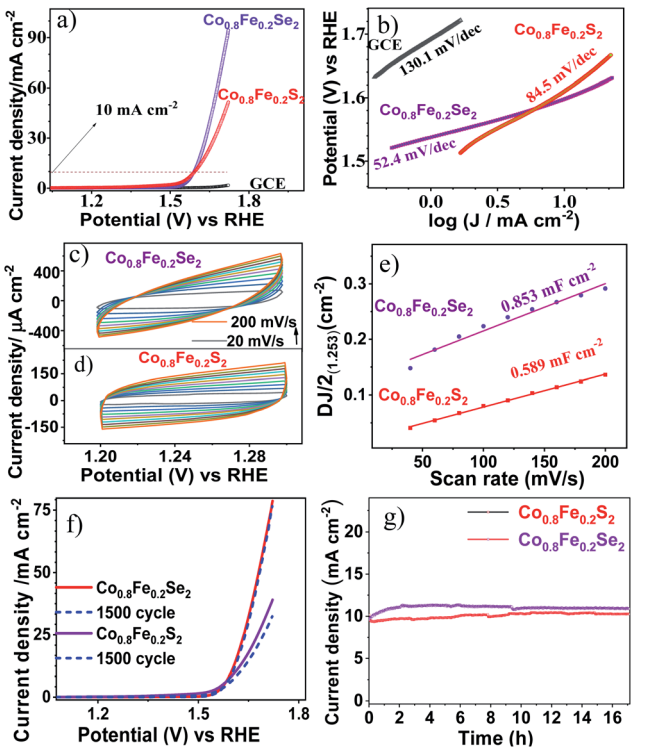

Fig. 7 (a) LSV curves, (b) Tafel plots, (c and d) C_{dl} measurements, (e) ECSA measurements, (f) stability of electro catalysts and (g) chronoamperometric (J–V) measurements in 1 M KOH of $Co_{0.8}Fe_{0.2}S_2$ and $Co_{0.8}Fe_{0.2}Se_2$.

(84.5 mV dec^{-1}) are very smaller than bare GCE (130.1 mV dec^{-1}). The observed values of over potential and Tafel slopes obtained for our materials ($Co_{0.8}Fe_{0.2}Se_2$ and $Co_{0.8}Fe_{0.2}S_2$) are superior to the reported ones as shown in Table 1. In general, this robust OER could have resulted from unique surface behaviours, multicomponent synergistic environments and unique morphology of electro active sites, which leads to improved electron transport and enhanced current densities.[16,17,34,40–42]

For superior electro catalysis, the materials should obtain higher current densities with lower over potential and Tafel values, which is observed here for $Co_{0.8}Fe_{0.2}Se_2$, confirming it better electro catalyst than $Co_{0.8}Fe_{0.2}S_2$ and bare GCE. Moreover, the insight into electrode kinetics of modified electrodes is evaluated using double-layer capacitance (C_{dl}) and electrochemical surface area (ECSA). Generally, ECSA is directly proportional to C_{dl} values. The C_{dl} measurements of $Co_{0.8}Fe_{0.2}Se_2$ and $Co_{0.8}Fe_{0.2}S_2$ (Fig. 7c and d) using cyclic voltammetry are carried with various scan rates from 0.02 to 0.002 V s^{-1} in 1 M KOH solution. $Co_{0.8}Fe_{0.2}Se_2$ possesses an excellent C_{dl} value than $Co_{0.8}Fe_{0.2}S_2$, hence higher value of ECSA of 0.853 mF cm^{-2} for $Co_{0.8}Fe_{0.2}Se_2$ than 0.589 mF cm^{-2} for $Co_{0.8}Fe_{0.2}S_2$ (Fig. 7e). Therefore, the higher C_{dl} value of $Co_{0.8}Fe_{0.2}Se_2$ is evidence of having an enormous number of active catalytic sites and high surface area of $Co_{0.8}Fe_{0.2}Se_2$ catalyst, resulting in enhanced electro catalytic performance.

In addition, the electro catalytic durability of both $Co_{0.8}Fe_{0.2}S_2$ and $Co_{0.8}Fe_{0.2}Se_2$ hybrid electro catalysts are evaluated through continuous 1500 CV cycling measurements (Fig. 7f). These experiments showed $Co_{0.8}Fe_{0.2}Se_2$ has negligible current density loss than $Co_{0.8}Fe_{0.2}S_2$ after 1500 CV cycles measurements, which indicates the high electro catalytic stability of $Co_{0.8}Fe_{0.2}Se_2$. To evaluate the electro catalytic stability of $Co_{0.8}Fe_{0.2}S_2$ and $Co_{0.8}Fe_{0.2}Se_2$, we have conducted chronoamperometry (i–t) studies (Fig. 7g). The chronoamperometry (i–t) studies of $Co_{0.8}Fe_{0.2}S_2$ and $Co_{0.8}Fe_{0.2}Se_2$ shows that the materials are stable for more than 18 h of activity. The current density of the electro catalyst was identified to be almost equal for a long time. The small sudden change in the current density at 8–10 h was due to the bubble formation, which blocks the active site, and then it remained stable upto 18 hours.

Remarkably, these results emphasize that $Co_{0.8}Fe_{0.2}Se_2$ and $Co_{0.8}Fe_{0.2}S_2$ produced through our HMDS assisted one-pot approach can perform as a class of efficient catalysts in alkaline OER electro catalysis. Consequently, exceptionally high surface area and mesoporous behaviours resulting from our novel approach of producing $Co_{0.8}Fe_{0.2}Se_2$ and $Co_{0.8}Fe_{0.2}S_2$, have made them suitable candidates to achieve effective redox kinetics. Besides the above factors, the template free approach leads to the easy access of substrates towards the active sites on catalysts surface, resulting in enhanced performances.[67] Thus, the decreased charge transport barriers led to good OER performance.

3.6. Electrochemical Cr(VI) reduction using $Co_{0.8}Fe_{0.2}S_2$ and $Co_{0.8}Fe_{0.2}Se_2$

For electrochemical Cr(VI) reduction, the nature of the electrolytic medium is an essential criterion. The acidic medium is suggested to be the best-suited media for carrying Cr(VI) reduction to Cr(III).[78] Therefore, we have performed the electro catalytic reduction of Cr(VI) in different acidic media (H_2SO_4, HNO_3 and HCl) having similar pH. The Fig. 6c and d represents the CV of $Co_{0.8}Fe_{0.2}S_2$ and $Co_{0.8}Fe_{0.2}Se_2$ electro catalysts in 0.1 mM Cr(VI) concentration loaded on GCE in different acidic media. A well-defined CV curve for Cr(VI) reduction is obtained in HCl medium for both the electro catalysts in the potential window of 0.0 V to −0.2 V compared to H_2SO_4 and HNO_3 in similar conditions. Besides this, the maximum value of current is obtained for both the electrocatalysts in the HCl medium, indicating it as a suitable acidic medium to carry electrocatalytic Cr(VI) reduction.

The effect of different concentrations of Cr(VI) was studied to comprehend further understanding. The Fig. 6e and f show a substantial increase in current for Cr(VI) reduction when the Cr(VI) concentrations increase from 0.01 μM to 50 μM. The very characteristic current peak value shows a direct proportional relationship with Cr(VI) concentration at the potential window of 0.0 V to −0.2 V, indicating the reduction of Cr(VI) to Cr(III) increases. When the peak current is calibrated against the Cr(VI) concentration of 0.01 μM to 50 μM, a linear relation is observed

Table 1 Comparison of OER performance of cobalt–iron Chalcogenides prepared in present work with the OER performance of electrodes reported in the literature

Materials	Material form	Overpotential @ 10 mA cm^{-2} (mV)	Tafel slope (mV dec^{-1})	Electrolyte	Ref.
CoFeP	Powder	350	59	1 M KOH	69
CoS_2	Film	361	64	1 M KOH	70
Co_3S_4	Powder	360	84.7	1 M KOH	71
Co-NP	Powder	390		0.1 M KOH	72
$Co_{1-x}S$–N and S codoped graphene	Powder	371	63	0.1 M KOH	73
O doped CoS_2	Film	370	67	1 M NaOH	74
$CoS–Co(OH)_2$@aMoS_{2+x}	Film	380	68	1 M KOH	75
$NiCoS/Ti_3C_2T_x$	Powder	365	58.2	1 M KOH	76
Co_9S_8@CNFs	Powder	512	78	1 M KOH	77
$Co_{0.8}Fe_{0.2}Se_2$ and $Co_{0.8}Fe_{0.2}S_2$	Powder	345, 350	52.4, 84.5	1 M KOH	This work

with a correlation coefficient of 0.956 and 0.934 for $Co_{0.8}Fe_{0.2}S_2$ and $Co_{0.8}Fe_{0.2}Se_2$, respectively (Fig. S3a and b†). The limit of detection (LOD) of Cr(VI) based on the signal-to-noise ratio 3.3 was calculated as 0.159 μg L^{-1} and 0.196 μg L^{-1} for $Co_{0.8}Fe_{0.2}S_2$ and $Co_{0.8}Fe_{0.2}Se_2$, and observed that these limits are similar to the reported observation.[78] Furthermore, CVs with different scan rates for 10 μM Cr(VI) concentration were reported from the potential range of 20 mV s^{-1} to 200 mV s^{-1} in 0.1 M HCl using modified GCE electrode loaded with $Co_{0.8}Fe_{0.2}S_2$ and $Co_{0.8}Fe_{0.2}Se_2$ (Fig. S3c and d†). A slight negative shift is observed with the increase in scan rates, showing the Cr(VI) reduction reaction's irreversible nature.[79,80]

As described above, the electrochemical Cr(VI) reduction is best carried under an acidic medium, where it shows that the more is H^+ ions available, the more the chances of reduction. According to the reported literature explaining the mechanism for Cr(VI) reduction, it is found that Cr(VI) reduction involves one electron and one proton transfer at a time, resulting in the disproportionation of Cr(VI) to Cr(IV) and Cr(VI) species. The Cr(IV) disproportionate further with Cr(V) to Cr(III) and Cr(VI), and it continues until complete reduction to Cr(III) takes place.[78–80] The total number of electrons involved in the reduction process counts upto 3. Overall, in electrochemical Cr(VI) reduction to Cr(III), superior performance is observed for $Co_{0.8}Fe_{0.2}S_2$ electro catalyst compared to $Co_{0.8}Fe_{0.2}Se_2$. This might be probably due to the effect of morphology involving spherical materials as a best suited for Cr(VI) reduction where maximum of Cr(VI) ions get adsorbed on the surface than in case flower shaped selenium materials.

4. Conclusions

In this work, a pair of transition metal (Co, Fe) based metal chalcogenides ($Co_{0.8}Fe_{0.2}S_2$ and $Co_{0.8}Fe_{0.2}Se_2$) were synthesized using the newly developed HMDS-assisted one-pot synthesis method. The synthesized materials were characterized by a series of comprehensive physicochemical characterization tools. The electro catalytic water splitting for OER showed that the synthesized materials could serve as robust electro catalysts. The material $Co_{0.8}Fe_{0.2}Se_2$ showed superior OER activity than $Co_{0.8}Fe_{0.2}S_2$ as indicated by the low overpotential and Tofel values (345 and 350 mV η @ 10 ms A cm^{-2}, 52.4 and 84.5 mV dec^{-1} for $Co_{0.8}Fe_{0.2}Se_2$ and $Co_{0.8}Fe_{0.2}S_2$, respectively). The electrochemical Cr(VI) reduction to Cr(III) further explains the bifunctional catalytic ability of $Co_{0.8}Fe_{0.2}S_2$ and $Co_{0.8}Fe_{0.2}Se_2$, where a maximum current and lower LOD is observed for $Co_{0.8}Fe_{0.2}S_2$ as compared to $Co_{0.8}Fe_{0.2}Se_2$. The materials showed potential to be excellent bifunctional electro catalysts for OER and Cr(VI) reduction.

Author contributions

Manzoor Ahmad Pandit, Dasari Sai Hemanth Kumar – data curation, formal analysis, investigation, methodology, writing – original draft. Krishnamurthi Muralidharan – conceptualization, supervision, funding acquisition, writing – review & editing. Manigandan Ramadoss, Yuanfu Chen – methodology, validation, visualization.

Conflicts of interest

The authors declare no conflicts of interest.

Acknowledgements

M. A. P thanks to UGC-BSR for fellowship. We thank to Centre for Nano Science and Technology (for TEM) and School of Physics (for PXRD) University of Hyderabad. Financial and infrastructure support from the University Grants Commission, New Delhi, India (through the UPE and CAS programs) and the Department of Science and Technology, New Delhi, India (through the PURSE and FIST programs) are gratefully acknowledged.

References

1 M.-T. Chen, R.-L. Zhang, J.-J. Feng, L.-P. Mei, Y. Jiao, L. Zhang and A.-J. Wang, A facile one-pot room-temperature growth of self-supported ultrathin rhodium-iridium nanosheets as high-efficiency electrocatalysts for hydrogen evolution reaction, *J. Colloid Interface Sci.*, 2022, **606**, 1707–1714.
2 M.-T. Chen, J.-J. Duan, J.-J. Feng, L.-P. Mei, Y. Jiao, L. Zhang and A.-J. Wang, Iron, rhodium-codoped Ni_2P nanosheets arrays supported on nickel foam as an efficient bifunctional electrocatalyst for overall water splitting, *J. Colloid Interface Sci.*, 2022, **605**, 888–896.
3 J. Ramkumar, Y. Chena, R. Manigandan, M. Karpuraranjith, B. Wang, W. Li and X. Zhang, A three-dimensional porous CoSnS@CNT nanoarchitecture as a highly efficient bifunctional catalyst for boosted OER performance and photocatalytic degradation, *Nanoscale*, 2020, **12**, 3879–3887.
4 U. Farooq, R. Phul, S. M. Alshehri, J. Ahmed and T. Ahmad, Electrocatalytic and Enhanced Photocatalytic Applications of Sodi-um Niobate Nanoparticles Developed by Citrate Precursor Route, *Sci. Rep.*, 2019, **9**, 4488.
5 M. Ramadoss, Y. Chen, Y. Hu, W. Li, B. Wang, X. Zhang, X. Wang and B. Yu, Three-dimensional Ni/Ni_3Fe embedded boron-doped carbon nano-tubes nanochain frameworks as highly efficient and durable electro-catalyst for oxygen evolution reaction, *J. Power Sources*, 2020, **451**, 227753.
6 X. Hu, T. Huang, Y. Tang, G. Fu and J. M. Lee, Three-dimensional graphene-supported Ni_3Fe/Co_9S_8 composites: rational design and active for oxygen reversible electrocatalysis, *ACS Appl. Mater. Interfaces*, 2019, **11**, 4028–4036.
7 L. Yang, S. Jiang, Y. Zhao, L. Zhu, S. Chen, X. Wang, Q. Wu, J. Ma, Y. Ma and Z. Hu, Boron-doped carbon nanotubes as metal-free electrocatalysts for the oxygen reduction reaction, *Angew. Chem., Int. Ed.*, 2011, **50**, 7132–7135.
8 Y. Yang, W. Zhang, Y. Xiao, Z. Shi, X. Cao, Y. Tang and Q. Gao, $CoNiSe_2$ heteronanorods decorated with layered-double-hydroxides for efficient hydrogen evolution, *Appl. Catal., B*, 2019, **242**, 132–139.

9 Y. Huan, J. Shi, G. Zhao, X. Yan and Y. Zhang, 2D Metallic Transitional Metal Dichalcogenides for Electrochemical Hydrogen Evolution, *Energy Technol.*, 2019, **7**, 1801025.

10 M. Yao, B. Sun, L. He, N. Wang, W. Hu and S. Komarneni, Self-Assembled Ni_3S_2 Nanosheets with Mesoporous Structure Tightly Held on Ni Foam as a Highly Efficient and Long-Term Electrocatalyst for Water Oxidation, *ACS Sustainable Chem. Eng.*, 2019, **7**, 5430–5439.

11 M. Gratzel, Recent Advances in Sensitized Mesoscopic Solar Cells, *Acc. Chem. Res.*, 2009, **42**, 1788–1798.

12 Z.-y. Li, K.-h. Ye, Q.-s. Zhong, C.-j. Zhang, S.-t. Shi and C.-w. Xu, Au–Co_3O_4/C as an Efficient Electrocatalyst for the Oxygen Evolution Reaction, *ChemPlusChem*, 2014, **79**, 1569–1572.

13 S. Ghosh, P. Kar, N. Bhandary, S. Basu, S. Sardar, T. Maiyalagan, D. Majumdar, S. K. Bhattacharya, A. Bhaumik, P. Lemmens and S. K. Pal, Microwave-assisted synthesis of porous Mn_2O_3 nanoballs as bifunctional electrocatalyst for oxygen reduction and evolution reaction, *Catal. Sci. Technol.*, 2016, **6**, 1417–1429.

14 Y. Jiang, X. Li, T. Wang and C. Wang, Enhanced electrocatalytic oxygen evolution of α-$Co(OH)_2$ nanosheets on carbon nanotube/polyimide films, *Nanoscale*, 2016, **8**, 9667–9675.

15 J.-X. Feng, H. Xu, Y.-T. Dong, S.-H. Ye, Y.-X. Tong and G.-R. Li, FeOOH/Co/FeOOH Hybrid Nanotube Arrays as High-Performance Electrocatalysts for the Oxygen Evolution Reaction, *Angew. Chem.*, 2016, **128**, 3758–3762.

16 J. O. Bockris and T. Otagawa, The Electrocatalysis of Oxygen Evolution on Perovskites, *J. Electrochem. Soc.*, 1984, **131**, 290–302.

17 M. R. Gao, Y. F. Xu, J. Jiang and S. H. Yu, Nanostructured metal chalcogenides: synthesis, modification, and applications in energy conversion and storage devices, *Chem. Soc. Rev.*, 2013, **42**, 2986–3017.

18 X. Zhang, Y. Chen, B. Wang, M. Chen, B. Yu, X. Wang, W. Zhang and D. Yang, FeNi nanoparticles embedded porous nitrogen-doped nanocarbon as efficient electrocatalyst for oxygen evolution reaction, *Electrochim. Acta*, 2019, **321**, 134720–134729.

19 D. Yang, W. Hou, Y. Lu, X. Wang, W. Zhang and Y. Chen, Scalable synthesis of bimetallic phosphide decorated in carbon nanotube network as multifunctional electrocatalyst for water splitting, *ACS Sustainable Chem. Eng.*, 2019, **7**, 13031–13040.

20 Y. Hu, B. Yu, M. Ramadoss, W. Li, D. Yang, B. Wang and Y. Chen, Scalable synthesis of heterogeneous W-W_2C nanoparticle-embedded CNT networks for boosted hydrogen evolution reaction in both acidic and alkaline media, *ACS Sustainable Chem. Eng.*, 2019, **7**, 10016–10024.

21 B. Zheng, Y. Chen, F. Qi, X. Wang, W. Zhang, Y. Li and X. Li, 3D-hierarchical $MoSe_2$ nanoarchitecture as a highly efficient electrocatalyst for hydrogen evolution, *2D Mater*, 2017, **4**, 025092.

22 M. Ramadoss, Y. Chen, Y. Hu and D. Yang, Three-dimensional porous nanoarchitecture constructed by ultrathin $NiCoBO_x$ nanosheets as a highly efficient and durable electrocatalyst for oxygen evolution reaction, *Electrochim. Acta*, 2019, **321**, 134666.

23 F. Xie, H. Wu, J. Mou, D. Lin, C. Xu, C. Wu and X. Sun, Ni_3N@Ni-Ci nanoarray as a highly active and durable non-noble-metal electrocatalyst for water oxidation at near-neutral pH, *J. Catal.*, 2017, **356**, 165–172.

24 N. I. Andersen, A. Serov and P. Atanassov, Metal oxides/CNT nano-composite catalysts for oxygen reduction/oxygen evolution in alkaline media, *Appl. Catal., B*, 2015, **163**, 623–627.

25 H. Li, Q. Zhou, F. Liu, W. Zhang, Z. Tan, H. Zhou, Z. Huang, S. Jiao and Y. Kuang, Biomimetic design of ultrathin edge-riched FeOOH@Carbon nanotubes as high-efficiency electrocatalysts for water splitting, *Appl. Catal., B*, 2019, **255**, 117755.

26 R. Huang, W. Chen, Y. Zhang, Z. Huang, H. Dai, Y. Zhou, Y. Wu and X. Lv, Well-designed cobalt-nickel sulfide microspheres with unique peapod-like structure for overall water splitting, *J. Colloid Interface Sci.*, 2019, **556**, 401–410.

27 J. Wang, W. Cui, Q. Liu, Z. Xing, A. M. Asiri and X. Sun, Recent Progress in Cobalt-Based Heterogeneous Catalysts for Electrochemical Water Splitting, *Adv. Mater.*, 2016, **28**, 215–230.

28 Y. Ge, J. Wu, X. Xu, M. Ye and J. Shen, Facile synthesis of $CoNi_2S_4$ and $CuCo_2S_4$ with different morphologies as prominent catalysts for hydrogen evolution reaction, *Int. J. Hydrogen Energy*, 2016, **41**, 19847–19854.

29 F. Zhang, Y. Ge, H. Chu, P. Dong, R. Baines, Y. Pei, M. Ye and J. Shen, Dual-Functional Starfish-like P-Doped Co−Ni−S Nanosheets Supported on Nickel Foams with Enhanced Electrochemical Performance and Excellent Stability for Overall Water Splitting, *ACS Appl. Mater. Interfaces*, 2018, **10**, 7087–7095.

30 C. Zequine, S. Bhoyate, F. Wang, X. Li, K. Siam, P. K. Kahol and R. K. Gupta, Effect of solvent for tailoring the nanomorphology of multinary $CuCo_2S_4$ for overall water splitting and energy storage, *J. Alloys Compd.*, 2019, **784**, 1–7.

31 H. Luo, H. Lei, Y. Yuan, Y. Liang, Y. Qiu, Z. Zhu and Z. Wang, Engineering Ternary Copper-Cobalt Sulfide Nanosheets as High-performance Electrocatalysts toward Oxygen evolution Reaction, *Catalysts*, 2019, **9**, 459.

32 B. B. Chen, D. K. Ma, Q. P. Ke, W. Chen and S. M. Huang, Indented Cu_2MoS_4 nanosheets with enhanced electrocatalytic and photocatalytic activities realized through edge engineering, *Phys. Chem. Chem. Phys.*, 2016, **18**, 6713–6721.

33 Y. Lin, S. Chen, K. Zhang and L. Song, Recent Advances of Ternary Layered Cu_2MX_4 (M = Mo, W; X = S, Se) Nanomaterials for Photocatalysis, *Sol. RRL*, 2019, **3**, 1800320.

34 B. Wang, Y. Hu, B. Yu, X. Zhang, D. Yang and Y. Chen, Heterogeneous CoFe–Co_8FeS_8 nanoparticles embedded in CNT networks as highly efficient and stable electrocatalysts for oxygen evolution reaction, *J. Power Sources*, 2019, **433**, 126688.

35 Y. Zhou, M. Luo, Z. Zhang, W. Li, X. Shen, W. Xia, M. Zhou and X. Zeng, Iron doped cobalt sulfide derived boosted

electrocatalyst for water Oxidation, *Appl. Surf. Sci.*, 2018, **448**, 9–15.

36 L. Huang, H. Wu, H. Liu and Y. Zhang, Phosphorous doped cobalt-iron sulfide/carbon nanotube as active and robust electrocatalysts for water splitting, *Electrochim. Acta*, 2019, **318**, 892–900.

37 T. Liu, F. Yang, G. Cheng and W. Luo, Reduced Graphene Oxide-Wrapped $Co_{9-x}Fe_xS_8$/Co,Fe-N-C Composite as Bifunctional Electrocatalyst for Oxygen Reduction and Evolution, *Small*, 2018, **14**, 1703748.

38 S. Shit, W. Jang, S. Bolar, N. C. Murmu, H. Koo and T. Kuila, Effect of Ion Diffusion in Cobalt Molybdenum Bimetallic Sulfide toward Electrocatalytic Water Splitting, *ACS Appl. Mater. Interfaces*, 2019, **11**, 21634–21644.

39 B. Quan, H. Tong, C. Liu, D. Li, S. Meng, M. Chen, J. Zhu and D. Jiang, Integration of $ZnCo_2S_4$ nanowires arrays with NiFe-LDH nanosheet as water dissociation promoter for enhanced electrocatalytic hydrogen evolution, *Electrochim. Acta*, 2019, **324**, 134861.

40 S. Chandrasekaran, L. Yao, L. Deng, C. Bowen, Y. Zhang, S. Chen, Z. Lin, F. Peng and P. Zhang, Recent advances in metal sulfides: from controlled fabrication to electrocatalytic, photocatalytic and photoelectrochemical water splitting and beyond, *Chem. Soc. Rev.*, 2019, **48**, 4178–4280.

41 X. Y. Yu and X. W. D. Lou, Mixed Metal Sulfides for Electrochemical Energy Storage and Conversion, *Adv. Energy Mater.*, 2018, **8**, 1701592.

42 G. Fu and J. M. Lee, Ternary metal sulfides for electrocatalytic energy Conversion, *J. Mater. Chem. A*, 2019, **7**, 9386–9405.

43 M. Shen, C. Ruan, Y. Chen, C. Jiang, K. Ai and L. Lu, Covalent Entrapment of Cobalt−Iron Sulfides in N-Doped Mesoporous Carbon: Extraordinary Bifunctional Electrocatalysts for Oxygen Reduction and Evolution Reactions, *ACS Appl. Mater. Interfaces*, 2015, **7**, 1207–1218.

44 S. Mani, S. Ramaraj, S. M. Chen, B. Dinesh and T. W. Chen, Two-dimensional metal chalcogenides analogous $NiSe_2$ nanosheets and its efficient electrocatalytic performance towards glucose sensing, *J. Colloid Interface Sci.*, 2017, **507**, 378–385.

45 Y.-R. Zheng, M.-R. Gao, Q. Gao, H.-H. Li, J. Xu, Z.-Y. Wu and S.-H. Yu, An Efficient CeO_2/$CoSe_2$ Nanobelt Composite for Electrochemical Water Oxidation, *Small*, 2015, **11**, 182–188.

46 R. J. Toh, C. C. M. Martinez, Z. Sofer and M. Pumera, $MoSe_2$ Nanolabels for Electrochemical Immunoassays, *Anal. Chem.*, 2016, **88**, 12204–12209.

47 L. Mi, H. Sun, Q. Ding, W. Chen, C. Liu, H. Hou, Z. Zheng and C. Shen, 3D hierarchically patterned tubular NiSe with nano-/microstructures for Li ion battery design, *Dalton Trans.*, 2012, **41**, 12595.

48 R. Xu, R. Wu, Y. Shi, J. Zhang and B. Zhang, Ni_3Se_2 nanoforest/Nifoam as a hydrophilic, metallic, and self-supported bifunctional electrocatalyst for both H_2 and O_2 generations, *nano energy*, 2016, **24**, 103–110.

49 A. Eftekhari, Molybdenum diselenide ($MoSe_2$) for energy storage, catalysis, and optoelectronics, *Applied Materials Today*, 2017, **8**, 1–17.

50 S. M. Tan, Z. Sofer, J. Luxa and M. Pumera, Aromatic-Exfoliated Transition Metal Dichalcogenides: Implications for Inherent Electrochemistry and Hydrogen Evolution, *ACS Catal.*, 2016, **6**, 4594–4607.

51 Z. Bo, S. Mao, Z. J. Han, K. Cen, J. Chen and K. Ostrikov, Emerging energy and environmental applications of vertically-oriented graphenes, *Chem. Soc. Rev.*, 2015, **44**, 2108–2121.

52 M. Gilic, M. Petrovic, J. Cirkovic, N. Paunovic, S. SavicSevic, Ž. Nikitovic, M. Romcevic, I. Yahia and N. Romcevic, Low-temperature photoluminescence of $CuSe_2$ nano objects in selenium thin films, *Process. Appl. Ceram.*, 2017, **11**, 127–135.

53 L. N. Qiao, H. C. Wang, Y. Shen, Y. H. Lin and C. W. Nan, Enhanced Photocatalytic Performance under Visible and Near-Infrared Irradiation of $Cu_{1.8}Se$/Cu_3Se_2 Composite via a Phase Junction, *Nanomaterials*, 2017, **7**, 19.

54 H. Xiao, S. Wang, C. Wang, Y. Li, H. Zhang, Z. Wang, Y. Zhou, C. An and J. Zhang, Lamellar structured $CoSe_2$ nanosheets directly arrayed on Ti plate as an efficient electrochemical catalyst for hydrogen evolution, *Electrochim. Acta*, 2016, **217**, 156–162.

55 M. Ramadoss, Y. Chen, Y. Hu, B. Wang, R. Jeyagopal, M. Karpuraranjith, X. Wang and D. Yang, Hierarchically porous nanoarchitecture constructed by ultrathin $CoSe_2$ embedded Fe-CoO nanosheets as robust electrocatalyst for water oxidation, *J. Mater. Sci. Technol.*, 2021, **78**, 229–237.

56 Z. F. Zhao, S. Shen, L. Cheng, L. Ma, J. Zhou, H. Ye, N. Han, T. Wu, Y. Li and J. Lu, Improved Sodium-Ion Storage Performance of Ultrasmall Iron Selenide Nanoparticles, *Nano Lett.*, 2017, **17**, 4137–4142.

57 M. Sakthivel, S. Ramaraja, S.-M. Chena, B. Dinesh, H. V. Ramasamy and Y. S. Lee, Entrapment of bimetallic $CoFeSe_2$ nanosphere in functionalized carbon nanofiber for selective and sensitive electrochemical detection of caffeic acid in wine samples, *Anal. Chim. Acta*, 2018, **1006**, 22–32.

58 Y. Jiang, X. Qian, Y. Niu, L. Shao, C. Zhu and L. Hou, Cobalt iron selenide/sulfide porous nanocubes as high-performance electrocatalysts for efficient dye-sensitized solar cells, *J. Power Sources*, 2017, **369**, 35–41.

59 M. A. Pandit, S. Billakanti and K. Muralidharan, A simplistic approach for the synthesis of CuS-CdS heterostructure: A Novel photo catalyst for oxidative dye degradation, *J. Environ. Chem. Eng.*, 2020, **8**, 103542.

60 J. R. Chiou, B. H. Lai, K. C. Hsu and D. H. Chen, One-pot green synthesis of silver/iron oxide composite nanoparticles for 4-nitrophenol reduction, *J. Hazard. Mater.*, 2013, **248**, 394–400.

61 M. A. Pandit, D. S. H. Kumar, S. Billakanti, M. Ramadoss and K. Muralidharan, Chalcopyrite with Magnetic and Dielectric Properties: An Introductory Catalyst for 4-Nitrophenol Reduction, *J. Phys. Chem. C*, 2020, **124**, 18010–18019.

62 G. A. Rather, A. Nanda, M. A. Pandit, S. Yahya, M. A. sofi, H. Barabadi and M. Saravanan, Biosynthesis of Zinc oxide

nanoparticles using Bergenia ciliate aqueous extract and evaluation of their photocatalytic and antioxidant potential, *Inorg. Chem. Commun.*, 2021, **134**, 109020.

63 B. Srinivas, M. A. Pandit and K. Muralidharan, Importance of Clean Surfaces on the Catalyst: SnS_2 Nanorings for Environmental Remediation, *ACS Omega*, 2019, **4**, 14970–14980.

64 M. V. Kovalenko, M. Scheele and D. V. Talapin, Colloidal Nanocrystals with Molecular Metal Chalcogenide Surface Ligands, *Science*, 2009, **324**, 1417–1420.

65 M. Ramadoss, Y. Chen, X. Chen, Z. Su, M. Karpuraranjith, D. Yang, M. A. Pandit and K. Muralidharan, Iron-Modulated Three-Dimensional CoNiP Vertical Nanoarrays: An Exploratory Binder-Free Bifunctional Electrocatalyst for Efficient Overall Water Splitting, *J. Phys. Chem. C*, 2021, **125**(38), 20972–20979.

66 B. G. Kumar and K. Muralidharan, Hexamethyldisilazane assisted synthesis of indium sulfide nanoparticles, *J. Mater. Chem.*, 2011, **21**, 11271–11275.

67 B. G. Kumar and K. Muralidharan, Organic free self-assembled copper sulfide microflowers, *Eur. J. Inorg. Chem.*, 2013, **2013**, 2102–2108.

68 R. Manigandan, T. Dhanasekaran, A. Padmanaban, K. Giribabu, R. Suresh and V. Narayanan, Bifunctional hexagonal Ni/NiO nanostructures: influence of the core–shell phase on magnetism, electrochemical sensing of serotonin, and catalytic reduction of 4-nitrophenol, *Nanoscale Adv.*, 2019, **1**, 1531–1540.

69 Y. Du, H. Qu, Y. Liu, Y. Han, L. Wang and B. Dong, Bimetallic CoFeP hollow microspheres as highly efficient bifunctional electrocatalysts for overall water splitting in alkaline media, *Appl. Surf. Sci.*, 2019, **465**, 816–823.

70 T. Liu, Y. Liang, Q. Liu, X. Sun, Y. He and A. M. Asiri, Electrodeposition of cobalt-sulfide nanosheets film as an efficient electrocatalyst for oxygen evolution reaction, *Electrochem. Commun.*, 2015, **60**, 92–96.

71 M. Zhu, Z. Zhang, H. Zhang, H. Zhang, X. Zhang, L. Zhang and S. Wang, Hydrophilic cobalt sulfide nanosheets as a bifunctional catalyst for oxygen and hydrogen evolution in electrolysis of alkaline aqueous solution, *J. Colloid Interface Sci.*, 2018, **509**, 522–528.

72 L. Wu, Q. Li, C. H. Wu, H. Zhu, A. Mendoza-Garcia, B. Shen, J. Guo and S. Sun, Stable Cobalt Nanoparticles and Their Monolayer Array as an Efficient Electrocatalyst for Oxygen Evolution Reaction, *J. Am. Chem. Soc.*, 2015, **137**, 7071–7074.

73 X. Qiao, J. Jin, H. Fan, Y. Li and S. Liao, In situ growth of cobalt sulfide hollow nanospheres embedded in nitrogen and sulfur co-doped graphene nanoholes as a highly active electrocatalyst for oxygen reduction and evolution, *J. Mater. Chem. A*, 2017, **5**, 12354–12360.

74 U. K. Sultana, T. He, A. Du and A. P. O'Mullane, An amorphous dual action electrocatalyst based on oxygen doped cobalt sulfide for the hydrogen and oxygen evolution reactions, *RSC Adv.*, 2017, **7**, 54995–55004.

75 T. Yoon and K. S. Kim, One-Step Synthesis of CoS-Doped β-$Co(OH)_2$@Amorphous MoS_{2+x} Hybrid Catalyst Grown on Nickel Foam for High-Performance Electrochemical Overall Water Splitting, *Adv. Funct. Mater.*, 2016, **26**, 7386–7393.

76 H. Zou, B. He, P. Kuang, J. Yu and K. Fan, Metal–Organic Framework-Derived Nickel–Cobalt Sulfide on Ultrathin Mxene Nanosheets for Electrocatalytic Oxygen Evolution, *ACS Appl. Mater. Interfaces*, 2018, **10**, 22311–22319.

77 H. Zhu, J. Zhang, R. Yanzhang, M. Du, Q. Wang, G. Gao, J. Wu, G. Wu, M. Zhang, B. Liu, J. Yao and X. Zhang, When Cubic Cobalt Sulfide Meets Layered Molybdenum Disulfide: A Core–Shell System toward Synergetic Electrocatalytic Water Splitting, *Adv. Mater.*, 2015, **27**, 4752–4759.

78 S. Aralekallu, M. Palanna, S. Hadimani, K. C. P. Prabhu, V. A. Sajjan, M. O. Thotiyl and L. K. Sannegowda, Biologically inspired catalyst for electrochemical reduction of hazardous hexavalent chromium, *Dalton Trans.*, 2020, **49**, 15061–15071.

79 C. M. Welch, O. Nekrassova and R. G. Compton, Reduction of hexavalent chromium at solid electrodes in acidic media: reaction mechanism and analytical applications, *Talanta*, 2005, **65**, 74–80.

80 R. T. Kachoosangi and R. G. Compton, Voltammetric determination of Chromium(VI) using a gold film modified carbon composite electrode, *Sens. Actuators, B*, 2013, **178**, 555–562.